Title

Structural and electronic properties of SrZrO3 and Sr(Ti,Zr) O3 alloys

Journal

Physical Review B - Condensed Matter and Materials Physics, 92(8)

ISSN

1098-0121

Authors

Weston, L
Janotti, A
Cui, XY
et al.

Publication Date

2015-08-11

DOI

10.1103/PhysRevB.92.085201

Peer reviewed

Structural and electronic properties of $SrZrO_3$ and $Sr(Ti,Zr)O_3$ alloys

L. Weston,[1,2] A. Janotti,[2] X. Y. Cui,[3] B. Himmetoglu,[2] C. Stampfl,[1] and C. G. Van de Walle[2]
[1]*School of Physics, The University of Sydney, Sydney, New South Wales 2006, Australia*
[2]*Materials Department, University of California, Santa Barbara, California 93106-5050, USA*
[3]*Australian Centre for Microscopy and Microanalysis, School of Aerospace, Mechanical and Mechatronic Engineering, The University of Sydney, New South Wales, 2006, Australia*
(Received 20 February 2015; published 11 August 2015)

Using hybrid density functional calculations, we study the electronic and structural properties of $SrZrO_3$ and ordered $Sr(Ti,Zr)O_3$ alloys. Calculations were performed for the ground-state orthorhombic (*Pnma*) and high-temperature cubic ($Pm3m$) phases of $SrZrO_3$. The variation of the lattice parameters and band gaps with Ti addition was studied using ordered $SrTi_x Zr_{1-x} O_3$ structures with $x = 0$, 0.25, 0.5, 0.75, and 1. As Ti is added to $SrZrO_3$, the lattice parameter is reduced and closely follows Vegard's law. On the other hand, the band gap shows a large bowing and is highly sensitive to the Ti distribution. For $x = 0.5$, we find that arranging the Ti and Zr atoms into a 1×1 $SrZrO_3/SrTiO_3$ superlattice along the [001] direction leads to interesting properties, including a highly dispersive single band at the conduction-band minimum (CBM), which is absent in both parent compounds, and a band gap close to that of pure $SrTiO_3$. These features are explained by the splitting of the lowest three conduction-band states due to the reduced symmetry of the superlattice, lowering the band originating from the in-plane Ti $3d_{xy}$ orbitals. The lifting of the t_{2g} orbital degeneracy around the CBM suppresses scattering due to electron-phonon interactions. Our results demonstrate how short-period $SrZrO_3/SrTiO_3$ superlattices could be exploited to engineer the band structure and improve carrier mobility compared to bulk $SrTiO_3$.

DOI: 10.1103/PhysRevB.92.085201 PACS number(s): 61.50.Ah, 71.20.Ps, 61.66.Dk

I. INTRODUCTION

$SrZrO_3$ (SZO) is a perovskite oxide of great interest as a high-temperature proton conductor [1,2]. SZO also exhibits resistance switching [3,4], strong luminescence [5], and ferroelectric ordering [6,7], making it a promising material for an array of technological applications. Recently, a two-dimensional electron gas (2DEG) has been achieved at the interface between $SrTiO_3$ (STO) and $Sr(Ti,Zr)O_3$ (STZO) via modulation doping [8], analogous to the traditional GaAs/(Al,Ga)As heterostructures which are widely used in high-electron-mobility transistors [9,10]. The conduction-band offset between STO and SZO has been calculated to be 1.7 eV [11], consistent with photoemission measurements [12] that produced a value of 1.9 eV. This value of the offset is large enough to confine a 2DEG entirely on the STO side [13]. Unfortunately, there is a large lattice mismatch (5%) between SZO and STO, posing severe limitations on the coherent epitaxial growth of pseudomorphic layers. One way to lessen the detrimental effects of the large lattice mismatch is to use STZO alloys instead of SZO as a barrier material [8]. Therefore, knowing the electronic and structural properties of STZO and how they compare to those of the parent compounds SZO and STO will be very useful for device design.

While STO prefers a cubic structure at room temperature, SZO is stable in an orthorhombic phase with *Pnma* symmetry (see Fig. 1). To date, most theoretical studies have focused on the high-temperature ($\geqslant$1440 K) cubic phase of SZO [14–16], while orthorhombic SZO has only been studied using density functional theory (DFT) within the standard local-density approximation (LDA) or generalized gradient approximation (GGA) [17,18]. While these approximations provide a reasonable description of the structural properties, they severely underestimate band gaps of semiconductors and insulators. On the other hand, hybrid functionals, such as the screened form proposed by Heyd, Scuseria, and Ernzerhof (HSE) [19,20], provide a much more accurate description of structural parameters and band gaps [21].

In this paper, we study the structural and electronic properties of cubic and orthorhombic SZO using the HSE hybrid functional. Engineering of the SZO band gap and lattice parameters by adding Ti is investigated using a series of $SrTi_x Zr_{1-x} O_3$ ordered alloys, with $x = 0$, 0.25, 0.5, 0.75, and 1. By adding Ti to SZO the lattice constant is reduced according to Vegard's law such that the lattice match with STO is improved. The band gap shows a strong bowing with Ti addition due to the interaction of the Ti $3d$ orbitals. As a consequence of this bowing, STZO with high Ti content would act as a poor barrier material for STO quantum wells. Finally, for STZO systems with 50% Ti concentration, whereby the Ti and Zr atoms can be arranged into an effective STO/SZO superlattice along the [001] direction, we find a single, highly dispersive band at the conduction-band minimum with d_{xy} character, and we discuss how this could lead to improved carrier mobility compared to bulk STO. Section II describes the methodology, and Sec. III contains our results and discussion.

II. COMPUTATIONAL DETAILS

The calculations are performed using density functional theory with the HSE hybrid functional [19,20]. In this approach, the short-range exchange potential is calculated by mixing nonlocal Hartree-Fock exchange with exchange from the generalized gradient approximation of Perdew, Burke, and Ernzerhof (PBE) [22]. The long-range exchange potential and the correlation potential are calculated with the PBE functional. The screening length and mixing parameter are fixed at 10 Å and 0.25, respectively [20]. For comparison we report both HSE and PBE results. The valence electrons are separated from the core by use of projector-augmented

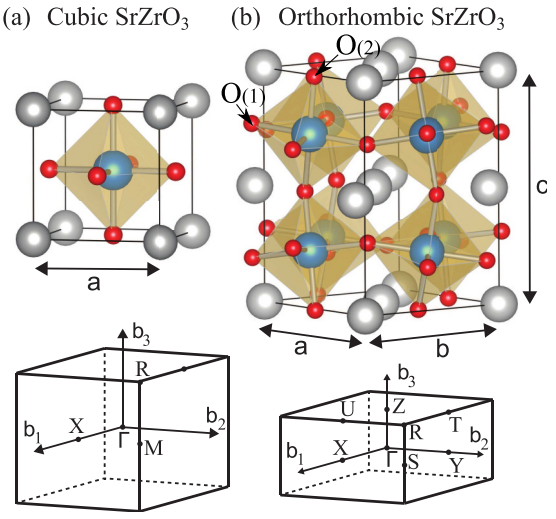

FIG. 1. (Color online) Bulk unit cells and Brillouin zones for the (a) cubic and (b) orthorhombic crystal structure of $SrZrO_3$. The lattice parameter a for the cubic phase and a, b, and c for the orthorhombic phase are indicated. The silver spheres represent Sr atoms, Zr are blue, and O are red; the inequivalent sites of O(1) and O(2) are indicated for the orthorhombic structure.

wave (PAW) pseudopotentials [23] as implemented in the VASP code [24]. For the present calculations we treated the Sr $4s^2 4p^6 5s^2$, Zr $4s^2 4p^6 4d^2 5s^2$, Ti $4s^2 3d^2$, and O $2s^2 2p^4$ electrons as valence electrons. The energy cutoff for the plane-wave basis set was 500 eV, with a k-point mesh of $7 \times 7 \times 7$ for the 5-atom cell and a $5 \times 5 \times 4$ mesh for the 20-atom cell.

III. RESULTS AND DISCUSSION

A. Bulk $SrZrO_3$

1. *Structural properties*

The unit cell of SZO in the cubic ($Pm3m$) perovskite crystal structure is shown in Fig. 1(a). The Sr atoms are located at the corners of the cubic unit cell and are surrounded by 12 nearest-neighbor O atoms. The Zr atom is located at the center of the unit cell and is sixfold coordinated to nearest-neighbor O atoms, forming an octahedron. The O atoms are found on the faces of the cubic unit cell and are twofold coordinated to neighboring Zr atoms. The primitive cell contains three O atoms which are equivalent by symmetry.

In Table I, we list the calculated lattice parameters of SZO in the cubic phase, obtained with the PBE and HSE functionals. The results are compared with previous calculations and with experiment. The lattice parameter calculated with PBE is 4.174 Å, while with HSE we obtain 4.141 Å. The reported experimental value is 4.154 Å [25], but we note that the cubic structure is stable only at temperatures in excess of 1440 K [26], and our calculations do not include the effect of thermal expansion. A quantitative estimate of the low-temperature lattice parameter for the cubic phase is difficult due to nonlinearities and phase changes, but we expect that both HSE and PBE somewhat overestimate the (low-temperature) lattice parameter, with HSE being closer to the experimental value.

Many perovskites, including SZO, prefer a distorted structure at room temperature, characterized by a tilting and rotation of the BO_6 octahedra [25]. For the orthorhombic phase, a 20-atom unit cell ($\sqrt{2}a \times \sqrt{2}a \times 2a$) is required to fully describe the lattice distortions, as shown in Fig. 1(b). The O atoms in the SZO orthorhombic structure, which has $Pnma$ symmetry, occupy two inequivalent sites, labeled O(1) and O(2). The ZrO_6 octahedron contains four O(1) sites, each having one short and one long Zr-O bond. In contrast, the O(2) site, of which there are two per ZrO_6 octahedron, is equidistant to both neighboring Zr atoms.

The calculated lattice parameters of SZO in the orthorhombic phase are also listed in Table I. The results using PBE are overestimated by about 1%, whereas the HSE results are in much better agreement with experiment. The HSE lattice parameters are 5.783, 5.828, and 8.195 Å, compared to the experimental values of 5.796, 5.817, and 8.205 Å [25,28–30]; the corresponding errors are 1.0%, 0.19%, and 0.12% for

TABLE I. Lattice parameters, band gaps, and enthalpies of formation ΔH_f for the cubic and orthorhombic phases of $SrZrO_3$, calculated with the PBE and HSE functionals. Results from previous calculations and from experiment are listed for comparison. For cubic $SrZrO_3$, the lattice parameter a is reported, as well as the direct (Γ-Γ) and indirect (R-Γ) band gaps. For orthorhombic SZO, the lattice constants (a, b, and c), as well as the direct (Γ-Γ) and indirect (S-Γ) band gaps, are reported.

						Band gap (eV)			
Structure	Methodology	Functional	a (Å)	b (Å)	c (Å)	Direct	Indirect	ΔH_f (eV)	Reference
Cubic	Present	PBE	4.174			3.62	3.31	−16.41	
		HSE	4.141			5.28	4.89	−17.15	
	Other DFT	LDA	4.095			3.62	3.37		[15]
		GGA	4.186			3.72	3.42		[16]
		B3LYP	4.144			5.07	4.89		[27]
	Experiment		4.154						[25]
Orthorhombic	Present	PBE	5.832	5.876	8.269	3.72	3.70	−16.64	
		HSE	5.783	5.828	8.195	5.36	5.33	−17.38	
	Other DFT	LDA	5.652	5.664	7.995	3.799	3.764		[17]
		GGA	5.812	5.870	8.243	3.77	3.75		[18]
	Experiment		5.796	5.817	8.205		5.2–5.6	−18.28	[25,28–30]

TABLE II. Atomic positions for $SrZrO_3$ in the orthorhombic structure, calculated with the PBE and HSE functionals and compared to experiment. The positions are presented as fractional coordinates with respect to the lattice vectors a, b, and c.

	Atomic coordinates (x,y,z)			
	Sr	Zr	O(1)	O(2)
PBE	0.006, 0.529, 0.25	0, 0, 0	0.072, 0.018, 0.25	0.214, 0.286, 0.038
HSE	0.006, 0.529, 0.25	0, 0, 0	0.071, 0.018, 0.25	0.214, 0.286, 0.037
Experiment[a]	0.004, 0.524, 0.25	0, 0, 0	0.069, 0.013, 0.25	0.215, 0.284, 0.036

[a]Reference [25].

the a, b, and c lattice parameters, respectively. In order to fully describe the distortions of the orthorhombic system, we report the inequivalent atomic positions of the primitive cell in Table II. The calculated atomic positions are also in good agreement with experiment [25]. We note that while PBE overestimates the lattice parameters, the distortions and atomic positions are captured very well, and the results presented in Table II are strikingly similar between PBE and HSE.

We also list the calculated enthalpies of formation ΔH_f of cubic and orthorhombic SZO in Table I. Both PBE and HSE functionals correctly predict that the orthorhombic phase is lower in energy than the cubic phase. The orthorhombic structure is about 0.23 eV per formula unit lower than that of the cubic structure. The HSE-calculated enthalpy of formation of −17.38 eV is in reasonable agreement with the experimental value of −18.28 eV [30]; in contrast, we find a much lower magnitude for the enthalpy of formation, −16.64 eV, using the PBE functional.

2. *Electronic properties*

The calculated fundamental and direct band gaps of SZO in the cubic and orthorhombic phases are also listed in Table I. Both the PBE and HSE calculations predict that cubic SZO has a fundamental indirect band gap R-Γ; the notation implies that the valence-band maximum (VBM) is at R and the conduction-band minimum (CBM) is at Γ. The calculated indirect band gap in PBE is 3.31 eV, and the direct gap at Γ is 3.62 eV, in agreement with previous calculations [15,16]. The HSE indirect gap R-Γ is 4.89 eV, and the direct gap at Γ is 5.28 eV. For the orthorhombic structure, both the PBE and HSE calculations predict an indirect band gap, with the VBM at S and the CBM at Γ. The direct band gap at Γ is only 0.02 eV (PBE) and 0.03 eV (HSE) larger than the indirect gap S-Γ. The fundamental gap is 3.70 eV in PBE and 5.33 eV in HSE. As expected, PBE severely underestimates the band gap. In contrast, the HSE value falls within the range of reported experimental values, 5.2–5.6 eV [28,29]. The larger gap of the orthorhombic phase, compared to that of the cubic structure, is attributed to narrower bandwidths as a consequence of the deviation of the Zr-O-Zr angles from 180°.

The HSE-calculated electronic band structures of cubic and orthorhombic SZO are shown in Fig. 2. The upper valence band of SZO is comprised mainly of O $2p$ states. In cubic SZO, the VBM is located at the R point, 0.31 eV higher in energy than at Γ, giving rise to the indirect band gap. The lower conduction band is comprised mostly of Zr $4d$ states which are split due to the crystal field. In the cubic phase, the crystal-field splitting results in the formation of a low-lying threefold-degenerate band, derived from the Zr $4d$ t_{2g} states, with the Zr $4d$ e_g band lying 4.6 eV higher in energy. The minimum of the t_{2g} conduction band is found at the Γ point. We note that inclusion of spin-orbit interaction (not shown) will split the Zr $4d$ t_{2g} bands into four- and twofold bands. The HSE-calculated spin-orbit splitting of the t_{2g} band is 69 meV.

The band structure of the SZO orthorhombic phase is plotted in Fig. 2(b). As in the cubic phase, the upper valence band is comprised of O $2p$ states. Orthorhombic SZO also

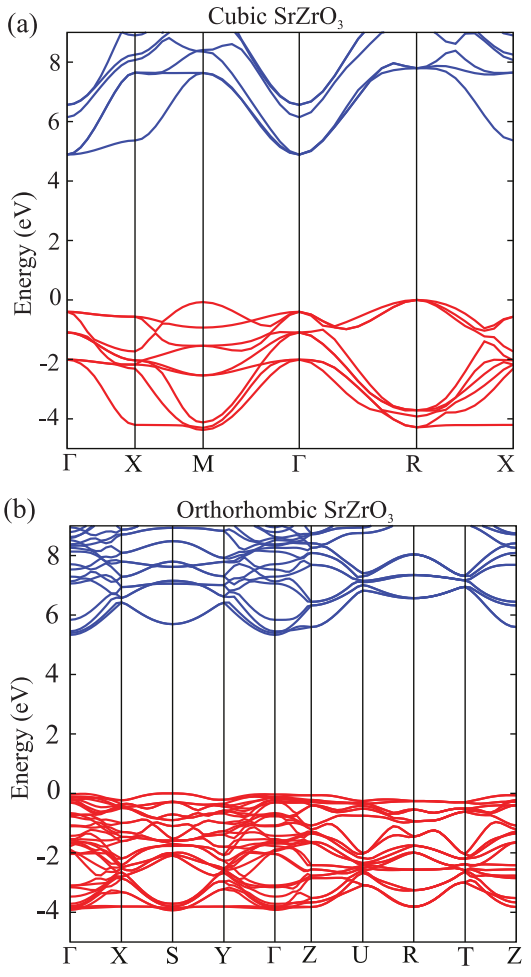

FIG. 2. (Color online) Calculated band structure of $SrZrO_3$ in the (a) cubic and (b) orthorhombic phases using the HSE functional. The zero of the energy axis is placed at the valence-band maximum in each case. Occupied states in the valence band are red; unoccupied states in the conduction band are blue.

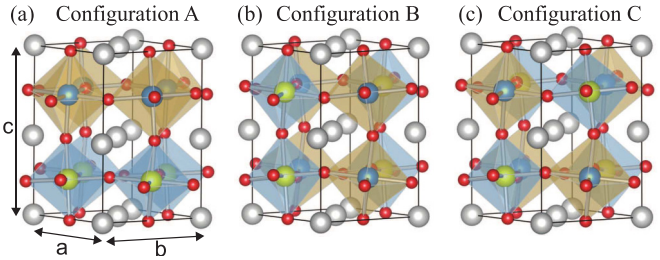

FIG. 3. (Color online) Three possible configurations (labeled A, B, and C) for the ordered $Sr(Ti,Zr)O_3$ alloys with 50% Ti concentration, based on a 20-atom orthorhombic cell. The silver spheres represent Sr atoms, Zr are blue, Ti are yellow, and O are red.

has an indirect band gap (S-Γ), but the VBM at the S point is only slightly higher in energy than at Γ. The lower conduction band is comprised of Zr 4d states. The degeneracy of the lower-lying t_{2g} band is lifted by the lattice distortion, but the splitting within the t_{2g} band is quite small: the second and third lowest conduction bands lie 65 and 121 meV above the CBM at the Γ point.

B. $Sr(Ti,Zr)O_3$ alloys

The orthorhombic primitive cell of SZO (Fig. 1) contains four Zr atoms. In the present study, the $Sr(Ti,Zr)O_3$ alloys are constructed by replacing up to four Zr with Ti atoms, resulting in concentrations of 0%, 25%, 50%, 75%, and 100%. In the cases of 25% and 75% Ti, there is only one possible unique configuration of the Ti atoms since all four Zr sites are equivalent. For 50% Ti concentration, there are three possible configurations, which we refer to as configurations A, B, and C. For each of these configurations, as shown in Fig. 3, the positions of the Ti atoms in the orthorhombic unit cell are A, $Ti_1(a/2,0,c/4)$, $Ti_2(0,b/2,c/4)$; B, $Ti_1(a/2,0,c/4)$, $Ti_2(a/2,0,3c/4)$; and C, $Ti_1(a/2,0,c/4)$, $Ti_2(0,b/2,3c/4)$. These are only nominal positions, and the internal distortions of the orthorhombic SZO structure lead to deviations from these coordinates. These positions correspond to Ti separations of $\sqrt{(\frac{a}{2})^2+(\frac{b}{2})^2}$ for configuration A, $c/2$ for B, and $\sqrt{(\frac{a}{2})^2+(\frac{b}{2})^2+(\frac{c}{2})^2}$ for C. All the lattice parameters and atomic positions are allowed to relax. We find that the Ti configuration with the largest Ti-Ti separation (configuration C) has the lowest energy, by 70 and 256 meV (per 20-atom cell) compared to configurations A and B, respectively. We note that larger supercells would be needed to find the ground-state configuration for the alloy in thermodynamic equilibrium [31]; however, our goal is to investigate $Sr(Ti,Zr)O_3$ alloys to be used as a barrier material for STO quantum wells, whereby the epitaxy of these systems is achieved using layer-by-layer growth techniques such as molecular beam epitaxy or pulsed laser deposition [8], where structures other than the minimum-energy configuration can be realized.

In Table III, we list the lattice parameters, bond angles, and band gaps of STZO alloys as a function of Ti concentration. We also list the in-plane pseudocubic lattice parameter of the orthorhombic STZO structure, defined as $a_c = \sqrt{(a^2+b^2)/2}$. The structures presented for pure SZO and STO are orthorhombic and cubic, respectively, as these are the ground-state phases at room temperature. Only the HSE results are reported. The

TABLE III. Lattice parameters (a,b, and c), bond angles, and band gaps E_g of $Sr(Ti,Zr)O_3$ as calculated with the HSE functional. Also reported is the pseudocubic lattice constant $a_c = \sqrt{(a^2+b^2)/2}$. For the bond angles, an average is taken over the supercell for the case of the low-symmetry $Sr(Ti,Zr)O_3$ alloys.

					Bond angle (°)		
% Ti	a	b	c	a_c	B–O(1)–B	B–O(2)–B	E_g
0	5.783	5.828	8.195	4.105	156.5	156.3	5.33
25	5.728	5.747	8.121	4.057	159.5	159.8	4.07
50 (A)	5.665	5.665	8.013	4.006	162.5	168.5	3.25
50 (B)	5.659	5.659	8.049	4.001	162.5	162.8	3.93
50 (C)	5.665	5.665	8.013	4.006	163.6	163.6	4.07
75	5.595	5.581	7.932	3.951	166.7	168.0	3.27
100	5.527	5.527	7.816	3.908	180.0	180.00	3.09

lattice parameters of SZO are about 5% larger than those of STO; the variation of a_c closely follows Vegard's law as Ti is added to SZO (see Fig. 4), and the lattice parameter shows only a slight dependence on the Ti configuration at 50% composition. The reduction of the lattice constant with Ti addition makes STZO alloys a more suitable barrier material for STO quantum wells due to the reduced lattice mismatch.

The internal structure of the BO_6 octahedra is also affected as a result of Ti addition, which can be seen from the increase in the B–O–B bond angles (B = Ti, Zr). In the cubic structure of STO the Ti–O–Ti bond angles are 180°; however, in the distorted SZO structure the Zr–O–Zr angles are reduced due to the tilting and rotation of ZrO_6 octahedra. For pure SZO, the bond angles along the Zr–O(1)–Zr and Zr–O(2)–Zr bonds are 156.5° and 156.3°, respectively.

Once Ti is added, the symmetry is lowered, and the bond angles vary. The average of the bond angles over the whole supercell for each alloy system is presented in Table III, and it can been seen that the tilting and rotation of the BO_6 octahedra are systematically reduced with increasing Ti addition. At the

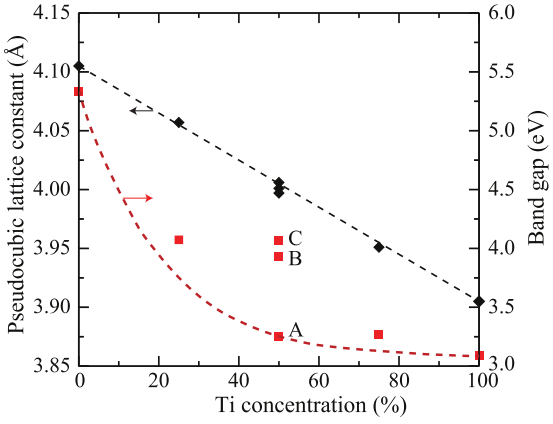

FIG. 4. (Color online) Variation of the pseudocubic in-plane lattice parameter (red squares and dashed line) and band gap (black diamonds and dashed line) of $Sr(Ti,Zr)O_3$ alloys as a function of Ti concentration. For 50% Ti concentration, the results for all three configurations (A, B, and C) are included. The data points represent calculated values, while the dashed lines only serve as a guide to the eye.

limit of 100% doping the bond angles are increased to 180° due to the cubic symmetry of pure STO. As mentioned above, the lower symmetry in the case of the STZO alloys leads to variation in the B–O–B bond angles; however, it is found that the variation about the mean is typically small (∼1°). There are several cases where the variation is much larger: for the 25% STZO alloy, the Ti–O(1)–Zr angles (163.3°) are 7.7° larger than the Zr–O(1)–Zr angles (155.6°), and similarly, for the 75% STZO alloy, the Ti–O(1)–Ti angles (171.6°) are 9.8° larger than the Ti–O(1)–Zr angles (161.8°). Additionally, for the 50% STZO alloy in configuration A, the in-plane Ti–O(1)–Ti angles (172.4°) are 20.3° larger than the Zr–O(1)–Zr angles (152.1°). The B–O(2)–B angles are fairly uniform throughout the cell in all cases.

The calculated band gap of SZO (5.33 eV) is significantly larger than the gap of 3.09 eV for STO. The band alignment of SZO/STO, as calculated in Ref. [11], is type I, with the VBM of SZO 0.34 eV lower than that of STO and the CBM of SZO 1.74 eV higher than that of STO, in agreement with experimental results based on photoelectron spectroscopy [12]. In Fig. 4 we show the variation of the band gap with Ti concentration. The band gap shows a significant bowing, as well as a strong dependence on the Ti configuration at 50% Ti concentration. The variation of the gap with Ti concentration indicates that low Zr content would lead to too small energy barriers. Specifically, for 75% Ti content the increase in the band gap from pure STO is only 0.18 eV. Decreasing the Ti content to 25% still leads to a band gap increase of only about 0.4 eV. The Ti content of the alloy can be reduced further, leading to a much larger increase in the band gap; however, this is at the expense of an increased lattice mismatch with pure STO.

The band gap of 50% STZO in configuration A is only slightly larger than the band gap of STO, but it is significantly lower than the gap of configurations B and C, by 0.7 and 0.8 eV, respectively. This large reduction in the band gap of configuration A is attributed to the directionality of the Zr/Ti d states. For the parent compounds SZO and STO, the lowest three conduction-band states originate from the d t_{2g} states (d_{xy},d_{xz},d_{yz}). SZO has a significantly larger band gap than STO because the Zr 4d states lie at a higher energy than the Ti 3d states. In configuration A, the structure is basically a 1 × 1 SZO/STO superlattice along the [001] direction, in which unit cells of SZO and STO alternate. In the STO layers, the Ti 3d_{xy} orbitals strongly interact in the in-plane directions, similar to the d_{xy} band in STO. This is evident in Fig. 5, where we plot the charge density of the lowest-energy conduction band (at Γ) for STZO in configuration A; the Ti 3d_{xy} character is clearly observed. Not surprisingly, this band lies at an energy similar to that of the CBM in STO (hence the similar band gap). On the other hand, for configurations B and C, the Ti orientation is such that the Ti 3d t_{2g} states have a greater interaction with Zr 4d states; consequently, the CBM is derived from a mixture of Ti 3d and Zr 4d states and lies much higher in energy than for configuration A.

The orbital composition of the lowest conduction-band states also explains the large bowing in the band gap of the STZO alloy. In the case of 25% Ti content, the t_{2g} states of the Ti 3d band hybridize predominantly with the Zr 4d_{xy} states of the in-plane Zr nearest neighbors and with the Zr 4$d_{xz/yz}$

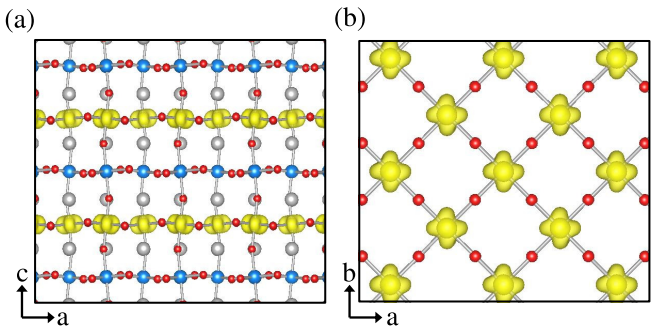

FIG. 5. (Color online) Charge-density isosurface of the lowest-energy conduction-band state at Γ for Sr(Ti,Zr)O_3 with 50% Ti concentration in configuration A, viewed along the (a) [010] and (b) [001] directions. The silver spheres represent Sr atoms, Zr are blue, Ti are yellow, and O are red. The isosurface is shown in yellow; the value of the isosurface is set to 12% of the maximum value. The system is effectively a 1 × 1 $SrZrO_3$/$SrTiO_3$ superlattice along the [001] direction, and the conduction-band minimum is confined to the $SrTiO_3$ layers with Ti 3d_{xy} character.

states of the out-of-plane Zr neighbors. The Ti 3d states have a significantly lower energy than the Zr 4d states, and at 25% Ti concentration there is already a large reduction in the gap with respect to pure SZO. For the 50% alloy in configurations B and C, the hybridization with neighboring Zr 4d states is comparable in degree to the 25% alloy, which is why the calculated band gap is similar. On the other hand, as discussed above, in configuration A the CBM has almost pure Ti 3d_{xy} character due to the strong in-plane coupling between these orbitals, so the band gap is reduced to near that of pure STO. Looking at the case of 75% Ti, the CBM is again composed mostly of Ti 3d t_{2g} states with almost no hybridization with Zr 4d states. As the 75% Ti alloy already has a CBM with nearly pure Ti 3d character, the band gap is nearly the same as that of pure STO. This bowing effect for the STZO structures is illustrated by the smooth curve in Fig. 4 passing through the value for the 50% Ti alloy in configuration A.

The 1 × 1 SZO/STO superlattice (configuration A) exhibits interesting properties, not present in the parent compounds. In Fig. 6 we show the calculated band structure for the 1 × 1 SZO/STO superlattice. First, it features a direct band gap, with a value (3.25 eV) that is close to that in STO (3.09 eV). Second, the lowest-energy conduction band is highly anisotropic almost dispersionless along the Γ-Z ([001]) direction due to the confinement of the electrons in the TiO_2 plane, yet it is highly dispersive in the in-plane directions due to the strong interaction of the Ti 3d_{xy} orbitals. The effective mass in the in-plane directions is found to be almost isotropic; the calculated masses are 0.45m_e along Γ-X and along Γ-S and 0.44m_e along Γ-Y. These values are similar to the effective mass of 0.39m_e calculated for the light electron band in bulk STO [32].

An important aspect of the electronic properties of the 1 × 1 SZO/STO superlattice is that it enables high electron mobility compared to STO. In STO, the electron mobility at room temperature is rather low as the presence of three bands around the CBM leads to enhanced electron-phonon scattering [33]. In contrast, in the 1 × 1 SZO/STO superlattice there exists only

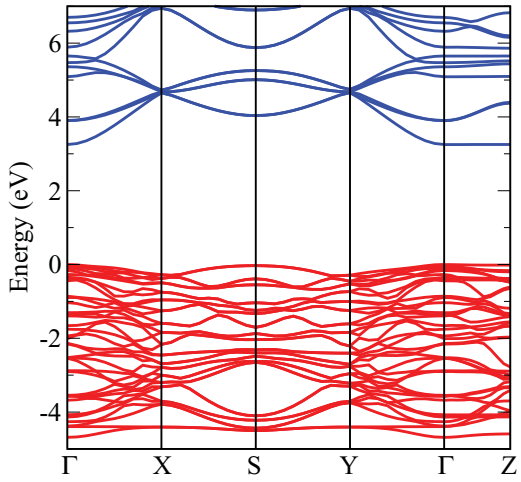

FIG. 6. (Color online) Electronic band structure calculated with HSE for $Sr(Ti,Zr)O_3$ with 50% Ti doping in configuration A. The zero of the energy axis is at the valence-band maximum. Valence-band states are red; conduction-band states are blue.

one band at the CBM that electrons can scatter to, leading to a significantly reduced scattering rate. Compared to the case of a threefold-degenerate band at the CBM, the presence of only a single band near the CBM reduces the electron-phonon scattering rate by more than a factor of 2 [33]. Finally, although the 1×1 SZO/STO superlattice (configuration A) is not the minimum-energy configuration for a 50% STZO alloy, it is only 70 meV higher in energy (per 20-atom cell) than the lowest-energy C configuration, making it very plausible that this structure could be realized using a layer-by-layer growth method, such as molecular beam epitaxy. Using modern techniques for oxide epitaxy, such oxide superlattices can now be realized with monolayer precision [34,35].

IV. SUMMARY

We have used hybrid density functional calculations to investigate the atomic and electronic structure of $SrZrO_3$ in the cubic and orthorhombic phases and $Sr(Ti,Zr)O_3$ ordered alloys. We find that the HSE hybrid functional provides improved accuracy when compared to the standard DFT-GGA calculations. In particular, HSE is able to accurately describe the band gap for the orthorhombic phase of $SrZrO_3$. For the $Sr(Ti,Zr)O_3$ ordered alloys, the lattice constant is reduced with increasing Ti content according to Vegard's law. The band gap of the alloy exhibits a large bowing with Ti addition, and consequently, only low-Ti alloys exhibit a significant band gap increase compared to pure $SrTiO_3$. In the case of alloys with 50% Ti content, we find that a 1×1 $SrZrO_3/SrTiO_3$ superlattice layered along the [001] direction exhibits highly interesting features, such as a direct band gap close to that of $SrTiO_3$ and a highly dispersive single band at the CBM with an effective mass similar to that of $SrTiO_3$, making it a promising material for enhancing carrier transport in perovskite titanates.

ACKNOWLEDGMENTS

This work was supported by the NSF MRSEC Program (DMR-1121053). L.W. was supported by the International Center for Materials Research (ICMR), an NSF-IMI Program (DMR08-43934), and by the Australian Research Council (ARC). X.Y.C. and C.S. also acknowledge support from the ARC. B.H. was supported by ONR (N00014-12-1-0976). Computational resources were provided by the Center for Scientific Computing at the CNSI and MRL (an NSF MRSEC, DMR-1121053, NSF CNS-0960316) and by the Extreme Science and Engineering Discovery Environment (XSEDE), supported by NSF (ACI-1053575).

[1] T. Yajima, H. Suzuki, T. Yogo, and H. Iwahara, Solid State Ionics **51**, 101 (1992).
[2] R. Davies, M. Islam, and J. Gale, Solid State Ionics **126**, 323 (1999).
[3] M.-H. Lin, M.-C. Wu, C.-Y. Huang, C.-H. Lin, and T.-Y. Tseng, J. Phys. D **43**, 295404 (2010).
[4] C.-C. Lin, B.-C. Tu, C.-C. Lin, C.-H. Lin, and T.-Y. Tseng, IEEE Electron Device Lett. **27**, 725 (2006).
[5] V. Jary, P. Bohacek, E. Mihokova, L. Havlak, B. Trunda, and M. Nikl, Opt. Mater. **35**, 1019 (2013).
[6] T. Tsurumi, T. Harigai, D. Tanaka, S. Nam, H. Kakemoto, S. Wada, and K. Saito, Appl. Phys. Lett. **85**, 5016 (2004).
[7] T. Harigai, S. Nam, H. Kakemoto, S. Wada, K. Saito, and T. Tsurumi, Thin Solid Films **509**, 13 (2006).
[8] A. P. Kajdos, D. G. Ouellette, T. A. Cain, and S. Stemmer, Appl. Phys. Lett. **103**, 082120 (2013).
[9] R. Dingle, H. L. Störmer, A. C. Gossard, and W. Wiegmann, Appl. Phys. Lett. **33**, 665 (1978).
[10] T. Mimura, S. Hiyamizu, T. Fujii, and K. Nanbu, Jpn. J. Appl. Phys. **19**, L225 (1980).
[11] L. Bjaalie, B. Himmetoglu, L. Weston, A. Janotti, and C. G. Van de Walle, New J. Phys. **16**, 025005 (2014).
[12] R. Schafranek, J. D. Baniecki, M. Ishii, Y. Kotaka, K. Yamanka, and K. Kurihara, J. Phys. D-Appl. Phys. **45**, 055303 (2012).
[13] P. Delugas, A. Filippetti, A. Gadaleta, I. Pallecchi, D. Marré, and V. Fiorentini, Phys. Rev. B **88**, 115304 (2013).
[14] R. Evarestov, A. Bandura, V. Alexandrov, and E. Kotomin, Phys. Status Solidi B **242**, R11 (2005).
[15] E. Mete, R. Shaltaf, and S. Ellialtioglu, Phys. Rev. B **68**, 035119 (2003).
[16] Z. Feng, H. Hu, S. Cui, and C. Bai, Solid State Commun. **148**, 472 (2008).
[17] R. Vali, Solid State Commun. **145**, 497 (2008).
[18] Q.-J. Liu, Z.-T. Liu, Y.-F. Liu, L.-P. Feng, H. Tian, and J.-G. Ding, Solid State Commun. **150**, 2032 (2010).
[19] J. Heyd, G. Scuseria, and M. Ernzerhof, J. Chem. Phys. **118**, 8207 (2003).
[20] J. Heyd, G. E. Scuseria, and M. Ernzerhof, J. Chem. Phys. **124**, 219906 (2006).

[21] M. Marsman, J. Paier, A. Stroppa, and G. Kresse, J. Phys. Condens. Matter **20**, 064201 (2008).
[22] J. P. Perdew, K. Burke, and M. Ernzerhof, Phys. Rev. Lett. **77**, 3865 (1996).
[23] P. E. Blöchl, Phys. Rev. B **50**, 17953 (1994).
[24] G. Kresse and J. Furthmüller, Phys. Rev. B **54**, 11169 (1996).
[25] B. J. Kennedy, C. J. Howard, and B. C. Chakoumakos, Phys. Rev. B **59**, 4023 (1999).
[26] D. de Ligny and P. Richet, Phys. Rev. B **53**, 3013 (1996).
[27] J. R. Sambrano, V. M. Longo, E. Longo, and C. A. Taft, J. Mol. Struct. THEOCHEM **813**, 49 (2007).
[28] Y. S. Lee, J. S. Lee, T. W. Noh, D. Y. Byun, K. S. Yoo, K. Yamaura, and E. Takayama-Muromachi, Phys. Rev. B **67**, 113101 (2003).
[29] A. Zhang, M. Lu, S. Wang, G. Zhou, S. Wang, and Y. Zhou, J. Alloys Compd. **433**, L7 (2007).
[30] M. Huntelaar, A. Booij, and E. Cordfunke, J. Chem. Thermodyn. **26**, 1095 (1994).
[31] D. Fuks, S. Dorfman, S. Piskunov, and E. A. Kotomin, Phys. Rev. B **71**, 014111 (2005).
[32] A. Janotti, D. Steiauf, and C. G. Van de Walle, Phys. Rev. B **84**, 201304 (2011).
[33] B. Himmetoglu, A. Janotti, H. Peelaers, A. Alkauskas, and C. G. Van de Walle, Phys. Rev. B **90**, 241204 (2014).
[34] D. Schlom, J. Haeni, J. Lettieri, C. Theis, W. Tian, J. Jiang, and X. Pan, Mater. Sci. Eng. B **87**, 282 (2001).
[35] C. A. Jackson, J. Y. Zhang, C. R. Freeze, and S. Stemmer, Nat. Commun. **5**, 4258 (2014).